Volume 4 | Number 19 | 21 May 2016 | Pages 7075–7504

Journal of Materials Chemistry A

Materials for energy and sustainability

www.rsc.org/MaterialsA

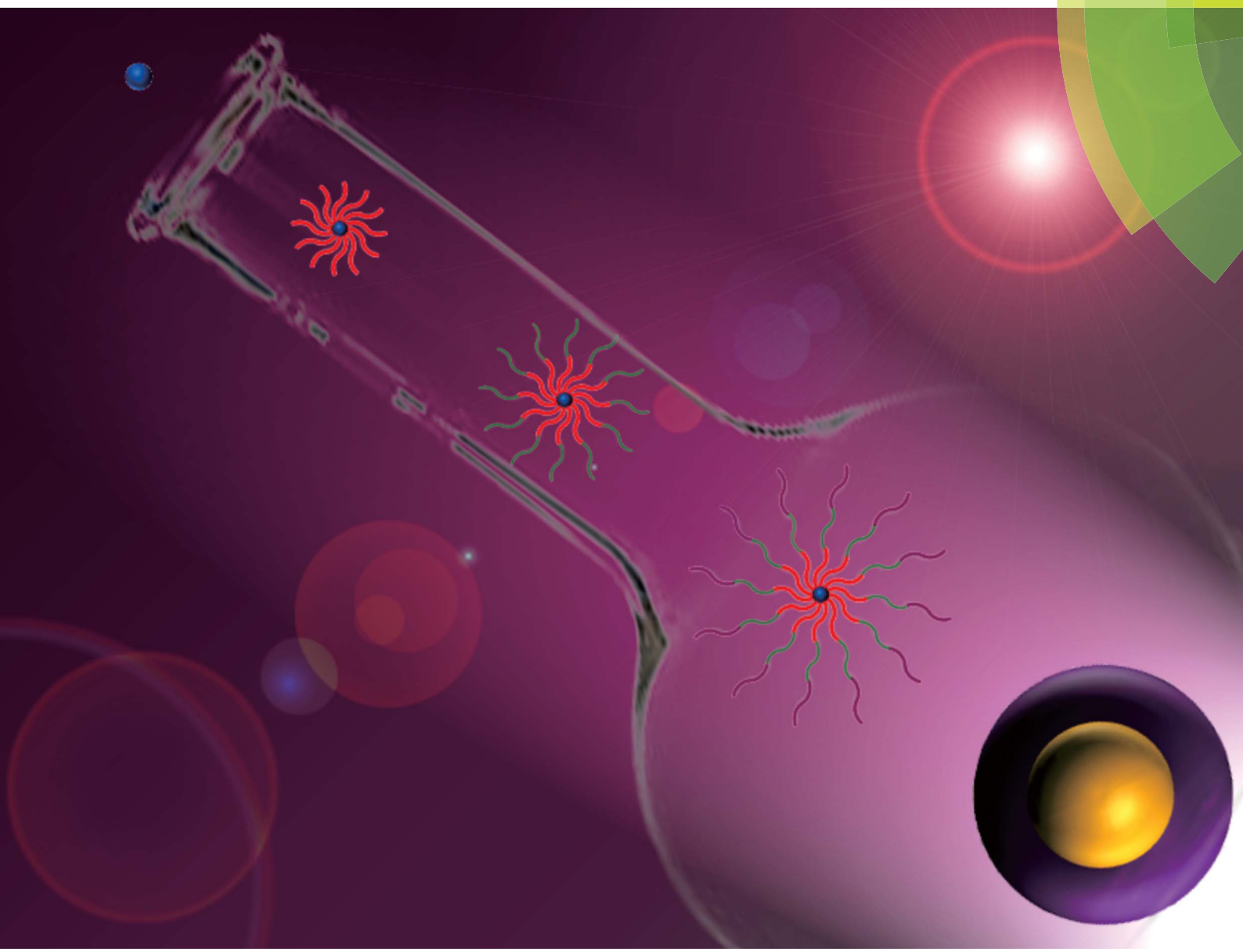

ISSN 2050-7488

ROYAL SOCIETY OF CHEMISTRY

PAPER

Changjian Lin, Zhiqun Lin *et al.*

Nonepitaxial growth of uniform and precisely size-tunable core/shell nanoparticles and their enhanced plasmon-driven photocatalysis

175 YEARS

Journal of Materials Chemistry A

PAPER

View Article Online
View Journal | View Issue

Cite this: J. Mater. Chem. A, 2016, 4, 7190

Nonepitaxial growth of uniform and precisely size-tunable core/shell nanoparticles and their enhanced plasmon-driven photocatalysis†

Mengye Wang,[ab] Xinchang Pang,[ab] Dajiang Zheng,[b] Yanjie He,[a] Lan Sun,[b] Changjian Lin*[b] and Zhiqun Lin*[a]

The ability to synthetically tune the size, shape, composition and architecture of inorganic nanostructures offers enormous opportunities to explore the fundamental structure–property relationships that occur uniquely at the nanoscale, and engineer greater functionality and design complexity into new material systems. Core/shell nanoparticles represent an important class of nanostructured materials that have garnered considerable interest. The success in producing core/shell nanoparticles with strictly controlled core diameter and shell thickness and tailoring their material properties relies crucially on the epitaxial growth of the shell material over the highly curved surface of the spherical core. However, effective methods to yield such high-quality core/shell nanoparticles are comparatively few and limited in scope. Here, we develop a robust nonepitaxial growth strategy to create uniform plasmonic/semiconducting core/shell nanoparticles with precisely controlled dimensions by capitalizing on amphiphilic star-like triblock copolymers as nanoreactors. The diameter of the plasmonic core and the thickness of the semiconductor shell can be independently and precisely regulated by tailoring the molecular weights (*i.e.*, the lengths) of the inner and intermediate blocks of star-like triblock copolymers, respectively. The successful crafting of plasmonic/semiconducting core/shell nanoparticles was corroborated by the composition and structural characterizations. These functional nanoparticles exhibited largely improved photocatalytic activities, which can be attributed to the localized surface plasmon-mediated light harvesting enhancement of the plasmonic core and the built-in internal electric field. This nonepitaxial growth strategy offers new levels of tailorability in the dimensions, compositions and architectures of nanomaterials with engineered functionalities for applications in catalytic, electronic, optic, optoelectronic and sensory materials and devices.

Received 2nd March 2016
Accepted 18th March 2016

DOI: 10.1039/c6ta01838f

www.rsc.org/MaterialsA

Introduction

Nanoparticles exhibit a wide range of unique properties that depend crucially on their size and shape, and are of both fundamental and practical interest. Breakthrough strategies that will facilitate the design and synthesis of a large diversity of nanocrystals with different properties and controllable size and shape in a simple and convenient manner are of key importance in advancing the use of nanocrystals for applications in light-weight structural materials, optics, electronics, photonics, optoelectronics, magnetic technologies, sensors, catalysis, drug delivery, biotechnology, and among other emerging fields.[1] Furthermore, core/shell structures that integrate the desired functionalities from both constituents offer a means of tailoring the properties of nanoparticles. It is noteworthy that current approaches to high-quality core/shell heterostructures are based on epitaxial growth, which requires moderate lattice mismatch between the two dissimilar materials. In particular, due to the presence of many different crystallographic facets on the highly curved surface of the spherical core[2] as well as the issues related to differences in crystal structure, bonding, and epitaxial growth sequence,[3] it is a grand challenge to achieve high-quality spherical core/shell nanoparticles with precisely controlled core diameter and shell thickness.

Noble metals such as Au and Ag nanoparticles often interact strongly with light through localized surface plasmon resonance (LSPR) as a result of the collective oscillations of free charges confined to the surface of noble metals.[4] They find a wide range of applications, including SPR-enabled light-harvesting enhancement for photocatalysis,[5] photovoltaics,[6] biological detection,[7] surface-enhanced Raman spectroscopy,[8] plasmonic integrated circuits,[9] and plasmonic lasers.[10] In order

[a]School of Materials Science and Engineering, Georgia Institute of Technology, Atlanta, GA 30332, USA. E-mail: zhiqun.lin@mse.gatech.edu

[b]Key Laboratory of Physical Chemistry of Solid Surfaces, College of Chemistry and Chemical Engineering, Xiamen University, Xiamen 361005, China. E-mail: cjlin@xmu.edu.cn

† Electronic supplementary information (ESI) available. See DOI: 10.1039/c6ta01838f

to utilize the full strength of LSPR, numerous studies have emerged to couple semiconductors of various structures (*e.g.*, nanotube arrays,[11] nanorods,[12] nanoparticles,[13] nanoshells,[14] *etc.*) with noble metal nanoparticles. Among them, metal/semiconductor core/shell nanoparticles are potential materials that possess promising attributes, for example size-dependent electronic and optical properties, for use in photocatalysis, optical and electronic devices, and solar energy conversion.[15] The size of noble metal nanoparticles can markedly influence the local field enhancement and thus affect the generation of electron–hole pairs in them.[13,16] In order to scrutinize the size effect, it is of paramount importance to produce plasmonic metal cores and semiconductor shells with narrow size distribution. However, precise tailoring of the core diameter and shell thickness remains challenging and has not yet been largely explored.

Herein, we report, for the first time, a viable and robust, nonepitaxial growth strategy for crafting uniform plasmonic/semiconducting core/shell nanoparticles (*i.e.*, Au/TiO_2) with precisely controlled dimensions by exploiting star-like triblock copolymers as nanoreactors. A multi-arm, star-like triblock copolymer, poly(4-vinyl pyridine)-*block*-poly(*t*-butyl acrylate)-*block*-poly(ethylene oxide) (denoted as P4VP-*b*-P*t*BA-*b*-PEO), composed of inner hydrophilic P4VP blocks, intermediate hydrophobic P*t*BA blocks and outer hydrophilic PEO blocks, was synthesized *via* a combination of sequential atom transfer radical polymerization (ATRP) of 4-vinyl pyridine (4VP) and *t*-butyl acrylate (*t*BA) and a click reaction from a β-cyclodextrin-based macroinitiator. The diameter of the Au core and the thickness of the TiO_2 shell can be accurately adjusted by tuning the molecular weights (*i.e.*, the lengths) of the inner P4VP and intermediate P*t*BA blocks, respectively, during the sequential ATRP of 4VP and *t*BA. The photocatalytic performance of Au/TiO_2 core/shell nanoparticles with judiciously varied Au core diameter and TiO_2 shell thickness was systematically explored. Quite intriguingly, compared to commercial TiO_2 nanoparticles (P25) and pure TiO_2 nanoparticles synthesized in a similar way to Au/TiO_2 nanoparticles, Au/TiO_2 nanoparticles demonstrated higher visible-light photocatalytic activities, which can be ascribed to the localized surface plasmon-mediated light harvesting enhancement and the built-in internal electric field.

Experimental section

Materials

2-Bromoisobutyryl bromide (98%), tris[2-(dimethylamino)ethyl] amine (Me_6-TREN, 97%), anhydrous 1-methyl-2-pyrrolidinone (99.5%), trifluoroacetic acid (TFA, 99.9%) and propargyl bromide solution (80 wt% in toluene) were purchased from Sigma-Aldrich, and used as received. CuBr (98%, Sigma-Aldrich) was stirred overnight in acetic acid, filtered, washed with ethanol and diethyl ether successively, and dried in a vacuum. β-Cyclodextrin (β-CD, Sigma-Aldrich) and poly(ethylene oxide) methyl ether (mPEO, M_n = 5000) were used as received. *tert*-Butyl acrylate (*t*BA, Sigma-Aldrich 98%), methyl ethyl ketone (Fisher Scientific, 99.9%) and *N*,*N*-dimethylformamide (DMF, Fisher Scientific, 99.9%) were distilled over CaH_2 under reduced pressure prior to use. Tetrahydrofuran (THF, 99%) was refluxed over potassium wire and distilled from potassium naphthalenide solution. 4-Vinylpyridine (4VP, Sigma-Aldrich 95%) was distilled over CaH_2 under reduced pressure prior to use. Diphenylmethyl sodium (DPMNa) (c = 0.52 M) was prepared according to the literature.[17] Gold(III) chloride trihydrate ($HAuCl_4 \cdot 3H_2O$, ≥99.9%), titanium(IV) isopropoxide (TTIP, ≥97.0%) and diphenyl ether (DPE, ≥99%) were purchased from Sigma-Aldrich, and used as received. All other reagents were purified by common purification procedures.

Preparation of the multi-arm, star-like P4VP-*b*-P*t*BA diblock copolymer end-functionalized with azide functional groups (*i.e.*, star-like P4VP-*b*-P*t*BA-N_3)

(a) Synthesis of multi-arm, star-like P4VP-Br. The star-like macroinitiator, 21Br-β-CD was prepared according to the previous report.[18,19] Sequentially, star-like poly(4-vinylpyridine) (P4VP) capped with bromine end groups (P4VP-Br) was prepared by atom transfer radical polymerization (ATRP) of the 4VP monomer in 2-propanol, using 21Br-β-CD with 21 ATRP initiation sites as the macroinitiator and CuBr/Me_6-TREN as the cocatalyst. Briefly, polymerization of 4VP was performed using 21Br-β-CD as the macroinitiator. An ampoule charged with CuBr (0.0707 g), Me_6-TREN (0.2271 g), 21Br-β-CD (0.1 g), 4VP (40 mL), and 40 mL of 2-propanol was vacuumed by three freeze–thaw-cycles in liquid nitrogen, then sealed and placed in an oil bath at 50 °C. The ampoule was taken out from the oil bath and dipped in an ice bath at different desired times to terminate the polymerization. The solution was then diluted with acetone and passed through a neutral alumina column to remove the catalyst, and precipitated in cold hexane. After filtration, the final product (*i.e.*, star-like P4VP-Br) was purified by the dissolution–precipitation process twice with chloroform and cold hexane and dried at 80 °C in a vacuum for 48 h.

(b) Synthesis of multi-arm, star-like P4VP-*b*-P*t*BA-Br. Multi-arm, star-like P4VP-*b*-P*t*BA was prepared by the ATRP of *t*BA monomer using the multi-arm, star-like P4VP-Br prepared above as a star-like macroinitiator (upper central panel in Scheme 1). The polymerization was performed in the ampoule. The reaction mixture (the molar ratio of *t*BA : star-like P4VP (*i.e.*, Br in the P4VP macroinitiator) : copper bromide : Me_6-TREN = 800 : 1 : 1 : 2) in methyl ethyl ketone (1 g *t*BA in 1 mL solvent) was degassed by three freeze–pump–thaw cycles in liquid nitrogen and then placed in a thermostatted oil bath maintained at 60 °C prior to polymerization. After a desired polymerization time, the mixture was dipped in an ice bath to terminate the reaction. The mixture was then diluted with chloroform and passed through a column of neutral alumina to remove the copper salt. The polymers were precipitated with an excess of cold methanol, filtered, and dried under vacuum to yield the multi-arm, star-like P4VP-*b*-P*t*BA diblock copolymer end-capped with bromine groups (star-like P4VP-*b*-P*t*BA-Br).

(c) Synthesis of multi-arm, star-like P4VP-*b*-P*t*BA-N_3. In order to obtain star-like P4VP-*b*-P*t*BA end-functionalized with azide groups (*i.e.*, star-like P4VP-*b*-P*t*BA-N_3), the purified star-like P4VP-*b*-P*t*BA-Br (4.0 g) was dissolved in DMF (15 mL), and

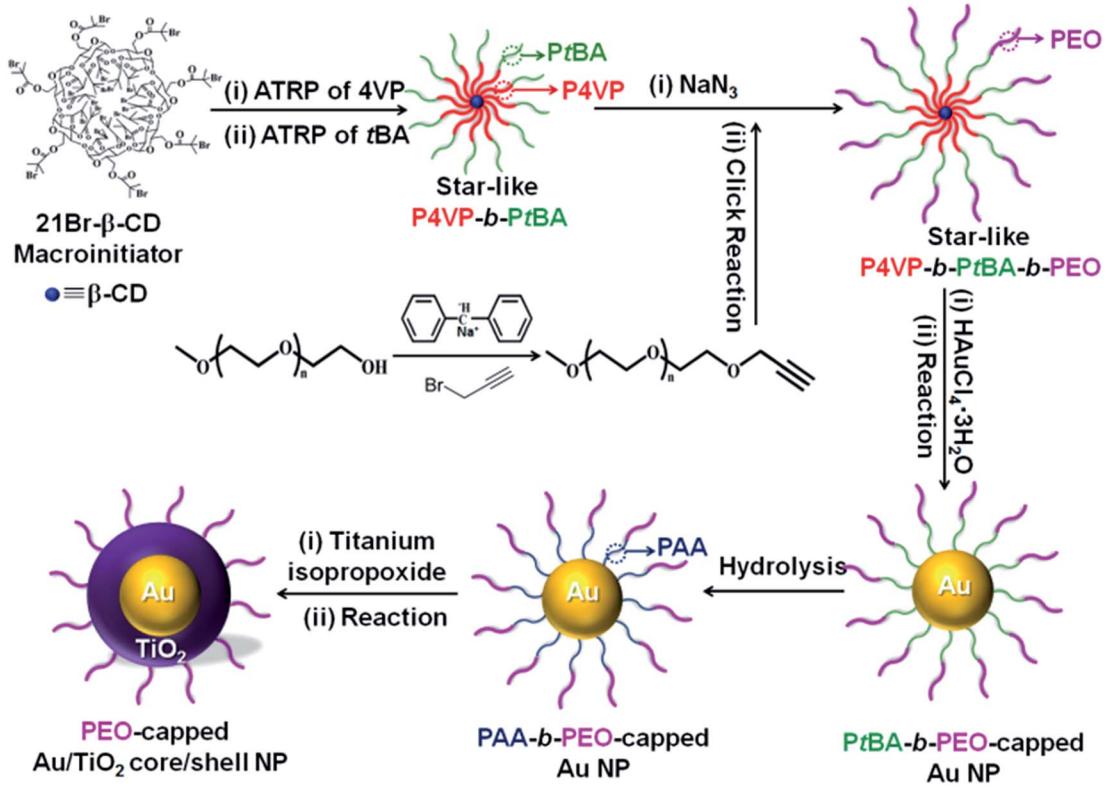

Scheme 1 Schematic stepwise representation of a robust synthesis route to uniform plasmonic/semiconducting Au/TiO_2 core/shell nanoparticles tethered with PEO chains on the surface.

sodium azide (Br in star-like P4VP-*b*-P*t*BA-Br : sodium azide = 1 : 10; molar ratio) was added to the solution. The reaction mixture was stirred for 24 h at room temperature. Dichloromethane (30.0 mL) was added to the mixture. The mixture was then washed with distilled water three times. The organic layer was dried with anhydrous $MgSO_4$, and the solvent was removed by drying in vacuum oven. The final product, star-like P4VP-*b*-P*t*BA-N_3, was collected and dried at 40 °C in a vacuum oven for 24 h.

Synthesis of alkyne-terminated mPEO (*i.e.*, mPEO-propargyl)

The end hydroxyl group of poly(ethylene oxide) methyl ether (mPEO, M_n = 5000) was modified by nucleophilic substitution into alkyne-terminated mPEO (*i.e.*, mPEO-propargyl) (central panel in Scheme 1).[1] Briefly, mPEO-OH (5.0 g, 1.0 mmol) and THF (60 mL) were added into a 250 mL dried ampoule. The system was then purged with argon. The DPMNa solution was introduced until the solution turned reddish-brown. After the ampoule was placed in an ice bath, propargyl bromide (5.0 mmol) was added dropwise for 2 h, and the reaction continued for 24 h at room temperature. The mPEO-alkyne was obtained by separation of the formed salts and precipitation in diethyl ether twice, and dried under vacuum at 40 °C until constant weight (3.65 g, yield: 73.0%). ^{1}H-NMR ($CDCl_3$) δ ppm: 2.44 (t, 1H, –$OCH_2C{\equiv}CH$), 4.20 (d, 2H, –$OCH_2C{\equiv}CH$), 3.38 (s, 3H, CH_3-O-PEO), 3.60–3.70 (m, –CH_2CH_2O– of PEO main chain).

Synthesis of multi-arm, star-like P4VP-*b*-P*t*BA-*b*-PEO by a click reaction

Star-like P4VP-*b*-P*t*BA-N_3 and alkyne-terminated PEO were dissolved in DMF (10 mL) in a dry ampoule. CuBr and Me_6-TREN were added, and the reaction mixture (PEO-alkyne : –N_3 in star-like P4VP-*b*-P*t*BA-N_3 : copper bromide : Me_6-TREN = 1.5 : 1 : 10 : 10; molar ratio) was degassed by three freeze–pump–thaw cycles in liquid nitrogen. The ampoule was first immersed in an oil bath at 90 °C for 24 h. The mixture was diluted with THF and passed through the alumina column to remove the copper salt. The product was precipitated in cold methanol and dried in a vacuum oven at 40 °C for 4 h, yielding the 21-arm, star-like P4VP-*b*-P*t*BA-*b*-PEO triblock copolymer (upper right panel in Scheme 1).

(a) Synthesis of plasmonic/semiconducting Au/TiO_2 core/shell nanoparticles. Plasmonic/semiconducting *Au/TiO_2 core/shell* nanoparticles were then produced by employing the star-like P4VP-*b*-P*t*BA-*b*-PEO triblock copolymer as the nanoreactor (*i.e.*, template). A certain amount of star-like P4VP-*b*-P*t*BA-*b*-PEO (molecular weights of the corresponding P4VP, P*t*BA, and PEO arms are listed in Table S1†) was dissolved in a mixture of dimethylformamide (DMF) and diphenyl ether (DPE) at DMF : DPE = 9 : 1 (by volume) at room temperature to form unimolecular micelles, followed by addition of an appropriate amount of $HAuCl_4$ (with ethanol as the reducer) that can be selectively incorporated into the compartment composed of inner star-like P4VP blocks *via* the strong coordination

interaction between pyridine groups in P4VP blocks of star-like P4VP-*b*-P*t*BA-*b*-PEO and the metal moieties of Au precursors ($HAuCl_4$). Such an interaction did not occur in the intermediate P*t*BA blocks and the outer PEO blocks as there were no active functional groups in both blocks to coordinate with precursors. Subsequent reduction of $HAuCl_4$ in the mixed solvents of DMF/DPE (= 9/1) at 60 °C for 10 h yielded Au core nanoparticles intimately capped by P*t*BA-*b*-PEO blocks (lower right panel in Scheme 1). The intermediate P*t*BA blocks were then hydrolyzed into poly(acrylic acid) (PAA) with trifluoroacetic acid (TFA), possessing carboxyl functional groups (lower central panel in Scheme 1). The TiO_2 shell was then synthesized using PAA blocks as the template. Typically, a certain amount of TiO_2 precursor, $Ti(OCH(CH_3)_2)_4$ (TTIP), was added to the reaction solution. Likewise, in the mixed solvents of DMF/DPE (= 9/1), the coordination interaction between the carboxyl groups of PAA blocks and the metal moieties of TTIP yielded the TiO_2 shell. After the reaction mixture was refluxed at 180 °C under argon for 2 h, the final product Au/TiO_2 core/shell nanoparticles intimately and permanently tethered with the outer hydrophilic PEO blocks as surface ligands were obtained (lower left panel in Scheme 1). The diameter of the Au core and the thickness of the TiO_2 shell can be precisely controlled by adjusting the length (*i.e.*, the molecular weight) of the first P4VP blocks and the second P*t*BA blocks, respectively. Finally, the samples were annealed at 500 °C in air for 2 h at a heating rate of 5 °C min^{-1} and a cooling rate of 2 °C min^{-1}.

(b) Synthesis of TiO_2 nanoparticles. For comparison, plain TiO_2 nanoparticles capped with PEO were also prepared by employing star-like PAA-*b*-PEO as templates.[1] First, similar to the previously described procedure, hydrophilic star-like PAA-*b*-PEO diblock copolymers with precisely tailorable molecular architectures were synthesized *via* a combination of the ATRP of *t*BA (P*t*BA-Br; and formation of P*t*BA-N_3 after end-functionalization with azide groups) and a click reaction between P*t*BA-N_3 and mPEO-propargyl. TiO_2 nanoparticles were then produced *via* the coordination interaction between the metal moieties of the TTIP precursor and the inner PAA blocks of the star-like PAA-*b*-PEO diblock copolymer. In a typical process, a certain amount of star-like PAA-*b*-PEO (the molecular weight of each PAA and PEO arm is 8.4k and 5k, respectively) was dissolved in a mixture of DMF and DPE at room temperature to form unimolecular micelles, followed by addition of an appropriate amount of TTIP that was preferentially incorporated into the regime comprising the inner PAA blocks as a result of strong coordination bonding as noted above. The solution was then refluxed at 180 °C under argon for 2 h, yielding TiO_2 nanoparticles with a diameter of approximately 10 nm capped with hydrophilic PEO.

Characterization

The PEO-capped Au/TiO_2 core/shell nanoparticles were imaged by transmission electron microscopy (TEM, JEOL 1200EX). The crystalline phase of the samples was measured by X-ray diffraction (XRD, X'pert PRO, The Netherlands). The optical absorption spectra of the as-prepared samples in chloroform were examined using a Shimadzu UV-2600 spectrophotometer.

Photocatalytic measurements

The visible-light photocatalytic activities of Au/TiO_2 nanoparticles and 10 nm TiO_2 nanoparticles (lower right panel in Scheme 1) after calcination at 500 °C in air for 2 h (*i.e.*, removing PEO chains and transforming amorphous TiO_2 into the anatase form) as noted above, as well as commercial TiO_2 nanoparticles (Degussa P25), were evaluated by the photo-degradation of Rhodamine B (RhB). The plain 10 nm TiO_2 nanoparticles (referred to as *homemade TiO_2* in order to differentiate from P25) and P25 were used as controls. The quartz glass photoreactor was equipped with a water jacket to control the reaction temperature. A 500 W tungsten-halogen lamp with an optical filter was employed as the light source, emitting visible light (>420 nm). The illumination intensity at the sample was 100 mW cm^{-2}. Au/TiO_2 nanoparticles after calcination at 500 °C in air (20 mg) were dispersed in 20 mL RhB aqueous solution (pH = 2.5, 5 mg L^{-1}) and allowed to reach adsorption/desorption equilibrium. All the measurements were conducted under continuous stirring and air was bubbled through the gas disperser into the reactor. The residual amount of RhB at various times was determined using the Shimadzu UV-2600.

Results and discussion

Synthesis of uniform and precisely size-tunable core/shell Au/TiO_2 nanoparticles

Conventional micelles derived from self-assembly of linear block copolymers in selective solvents are dynamically stable as the assembled structures depend sensitively on the concentration, solvent, pH, and temperature, among other parameters. In stark contrast, because of their branched yet compact architecture, amphiphilic star-like block copolymers with each arm covalently connected to the core form unimolecular micelles in solution.[18,20] Such unimolecular micelles are rather static.[21] They are monodisperse and structurally stable spherical macromolecules, which can thus be exploited as nanoreactors (*i.e.*, templates) to create functional inorganic nanoparticles *via* the coordination reaction between the functional groups of star-like block copolymers and metal moieties of precursors. As depicted in Scheme 1, the amphiphilic star-like P4VP-*b*-P*t*BA-*b*-PEO triblock copolymer (upper right panel) possessed precisely controllable molecular weight of each block (*i.e.*, the length) as it was synthesized by sequential ATRP (a living free radical polymerization technique) in conjunction with the click reaction. *Plasmonic/semiconducting Au/TiO_2 core/shell* nanoparticles (lower left panel in Scheme 1) were produced by capitalizing on the star-like P4VP-*b*-P*t*BA-*b*-PEO triblock copolymer as the template. The mixed solvents of dimethylformamide (DMF) and diphenyl ether (DPE) at a volume ratio of DMF : DPE = 9 : 1 were used in producing nanoparticles (see Methods). As DMF is a good solvent for all three blocks, while DPE is a poor solvent for P*t*BA and PEO blocks yet a good solvent for the P4VP block, a compact spherical macromolecule (*i.e.*, unimolecular micelle) composed of inner coil-like P4VP blocks and outer collapsed P*t*BA-*b*-PEO diblocks was formed. As a result, the Au precursor, $HAuCl_4$, preferentially entered the regime occupied by star-like

P4VP blocks and was converted into Au nanoparticles (*i.e.*, P*t*BA-*b*-PEO-capped Au nanoparticles) *via* the strong coordination interaction between pyridine groups in the P4VP block with Au^{3+} of $HAuCl_4$ (see Methods).

In order to form the TiO_2 shell, the intermediate hydrophobic P*t*BA blocks were hydrolyzed into hydrophilic poly(acrylic acid) (PAA) blocks (see Methods). Similarly, the use of the 9 : 1 ratio of DMF : DPE as the mixed solvents to perform the reaction induced the inner PAA blocks to retain the coil-like conformation, and the outer PEO blocks to collapse as DMF is a good solvent for PAA and PEO, and DPE is a good solvent for PAA but a poor solvent for PEO (*i.e.*, unfavorable interaction between PEO chains and DPE). A well-defined space comprising coil-like PAA blocks with collapsed PEO blocks situated outside PAA was thus obtained. The addition of the TiO_2 precursor, titanium(IV) isopropoxide (TTIP) yielded the TiO_2 shell (see Methods). Consequently, plasmonic/semiconducting *Au/TiO$_2$ core/shell* nanoparticles closely and permanently capped with PEO chains were obtained.

We note that the diameter of the Au core and the thickness of the TiO_2 shell can be easily controlled by tailoring the molecular weights (*i.e.*, the lengths) of the inner P4VP and intermediate P*t*BA blocks, respectively, during the sequential ATRP of 4VP and *t*BA. Most importantly, as the growth of the shell was fully templated by the hydrophilic PAA, the growth of the lattice structure of the shell can be completely independent of that of the core material, thereby circumventing the limitations imposed by epitaxial growth that is often needed for producing core/shell nanoparticles.

Fig. 1 compares the TEM images of the as-synthesized plasmonic Au core (lower right panel in Scheme 1) and plasmonic/semiconducting Au/TiO_2 core/shell nanoparticles with a fixed Au core diameter and varied TiO_2 shell thickness (lower left panel in Scheme 1). They were crafted by using the star-like P4VP-*b*-P*t*BA-*b*-PEO triblock copolymer as a nanoreactor before and after the hydrolysis of the intermediate P*t*BA block, respectively (Scheme 1). Notably, Au core and Au/TiO_2 core/shell nanoparticles are highly uniform (Table S2†). Monodisperse Au core nanoparticles with a diameter of 15 nm tethered with P*t*BA-*b*-PEO chains on the surface are shown in Fig. 1a. It is not surprising that through adjusting the molecular weights of the P*t*BA block alone, the thickness of the TiO_2 shell can be delicately regulated. Fig. 1b–d present Au/TiO_2 core/shell nanoparticles intimately and permanently capped with PEO chains with the Au core diameter and TiO_2 shell thickness of 15 nm and 1 nm (Fig. 1b), 15 nm and 5 nm (Fig. 1c), and 15 nm and 10 nm (Fig. 1d), respectively. The Au cores appeared darker and were surrounded by the lighter TiO_2 shells, as clearly evident by TEM imaging.

It is noteworthy that our strategy provides remarkable flexibility in synthesizing core/shell nanoparticles with tailored dimensions. Thus, on the other hand, by modulating the molecular weights of P4VP alone while retaining the molecular weight of P*t*BA, the diameter of the Au core can be precisely tuned at a fixed TiO_2 shell thickness (Table S3†). Fig. 2a and b display the 5 nm and 10 nm Au core nanoparticles, respectively. A set of Au/TiO_2 core/shell nanoparticles with varied diameters of Au cores and constant thickness of TiO_2 shell are shown in Fig. 2c (5 nm/5 nm), Fig. 2d (10 nm/5 nm), and Fig. 1c (15 nm/5 nm), respectively. A representative HRTEM image revealed that the TiO_2 shell in Au/TiO_2 (10 nm/5 nm) core/shell nanoparticles was amorphous (Fig. S1†). It is interesting to note that rather than physical adsorption or weak chemical tethering

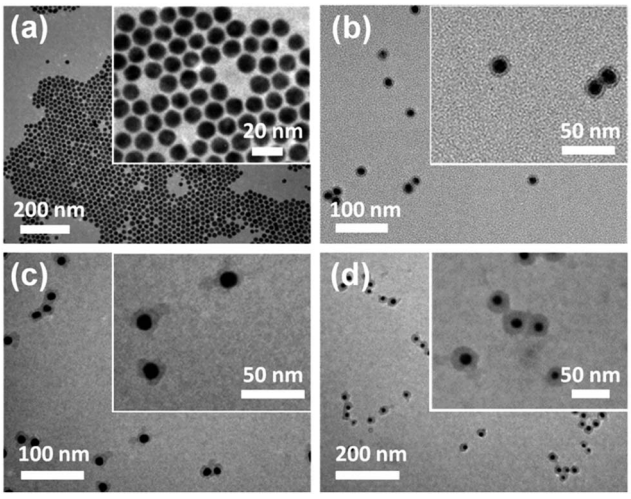

Fig. 1 TEM images of Au core nanoparticles and plasmonic/semiconducting Au/TiO_2 core/shell nanoparticles with a fixed core diameter and varied shell thickness. (a) Pure Au core nanoparticles with a diameter of 15 nm tethered with P*t*BA-*b*-PEO chains on the surface. (b–d) Au/TiO_2 core/shell nanoparticles capped with PEO chains on the surface. The diameter of the Au core and thickness of the TiO_2 shell are as follows: (b) 15 nm Au and 1 nm TiO_2, (c) 15 nm Au and 5 nm TiO_2, and (d) 15 nm Au and 10 nm TiO_2, respectively. The corresponding close-ups are shown as insets.

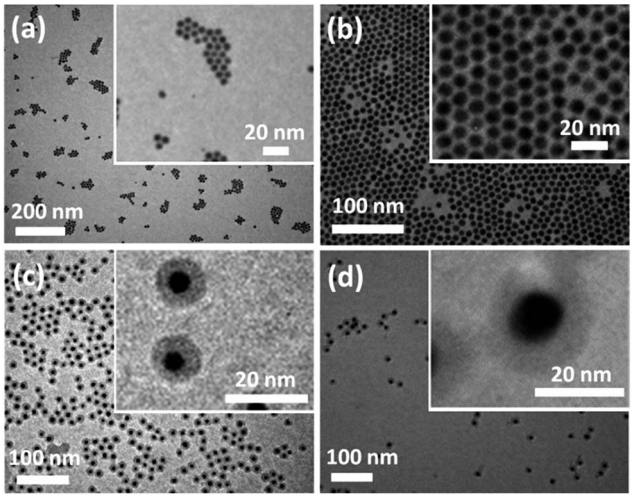

Fig. 2 TEM images of Au core nanoparticles with different diameters and plasmonic/semiconducting Au/TiO_2 core/shell nanoparticles with varied core diameter and constant shell thickness. (a and b) Pure Au core nanoparticles with a diameter of (a) 5 nm and (b) 10 nm tethered with P*t*BA-*b*-PEO chains on the surface. (c and d) Au/TiO_2 core/shell nanoparticles capped with PEO chains on the surface. The diameter of the Au core and the thickness of the TiO_2 shell are 5 nm Au and 5 nm TiO_2 for (c), and 10 nm Au and 5 nm TiO_2 for (d), respectively. The corresponding close-ups are shown as insets.

on the nanoparticle surface as in copious work in the literature, the surfaces of Au core and Au/TiO_2 core/shell nanoparticles were directly and permanently anchored by P*t*BA-PEO and PEO chains, respectively, thereby eliminating the possible adsorption and desorption of surface passivating ligands during storage, and imparting the long-term stability of the resulting nanoparticles.

The X-ray diffraction profiles of all as-prepared Au/TiO_2 nanoparticles capped with PEO chains showed only the characteristic peaks corresponding to Au (Fig. 3a), suggesting that the TiO_2 shell was amorphous. After sintering at 500 °C in air, the TiO_2 shell was transformed into the anatase form and the peak intensity of Au was enhanced due most likely to the removal of all the polymers, as revealed by XRD measurements (Fig. 3b).

Optical and photocatalytic measurement of core/shell Au/TiO_2 nanoparticles

Au/TiO_2 nanoparticles composed of the plasmonic core and semiconductor shell were then exploited to systematically elaborate the effects of Au core diameter and TiO_2 shell thickness on their photocatalytic performances. First, the diameter of the Au core was fixed at 15 nm, while the thickness of the TiO_2 shell was tuned from 1 nm to 5 nm to 10 nm (Fig. 1b–d). The localized surface plasmon resonance (LSPR) properties of the as-prepared samples were examined. The UV-vis absorption spectra of PEO-capped Au/TiO_2 nanoparticles are shown in Fig. 4a. As noted above, 15 nm Au nanoparticles capped with P*t*BA-*b*-PEO were also synthesized (lower right panel in Scheme 1; Fig. 1a) and used as control, exhibiting a LSPR maximum in between 520 and 525 nm (open star curve in Fig. 4a). Interestingly, compared to pure Au nanoparticles, the LSPR peaks for all three PEO-capped Au/TiO_2 nanoparticles with varied TiO_2 shell thickness were red-shifted. The surface plasmons are very sensitive to the change of dielectric environment on the metal surface. The red-shift of plasmonic absorption occurred due to the increase in the refractive index of the local dielectric environment of the Au core *via* theTiO_2 shell coating.[22] The presence of a thicker higher-refractive-index TiO_2 shell resulted in an

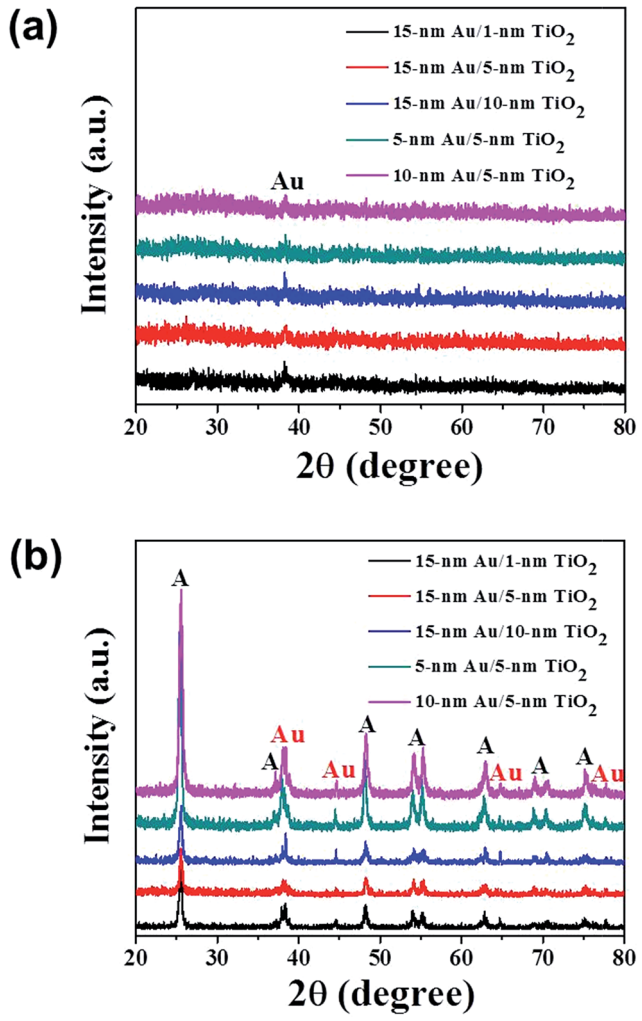

Fig. 3 XRD patterns of PEO-capped Au/TiO_2 core/shell nanoparticles before and after sintering at 500 °C in air. (a) As-prepared nanoparticles, and (b) after calcination at 500 °C in air (Au refers to the Au core, and A refers to the anatase TiO_2 shell).

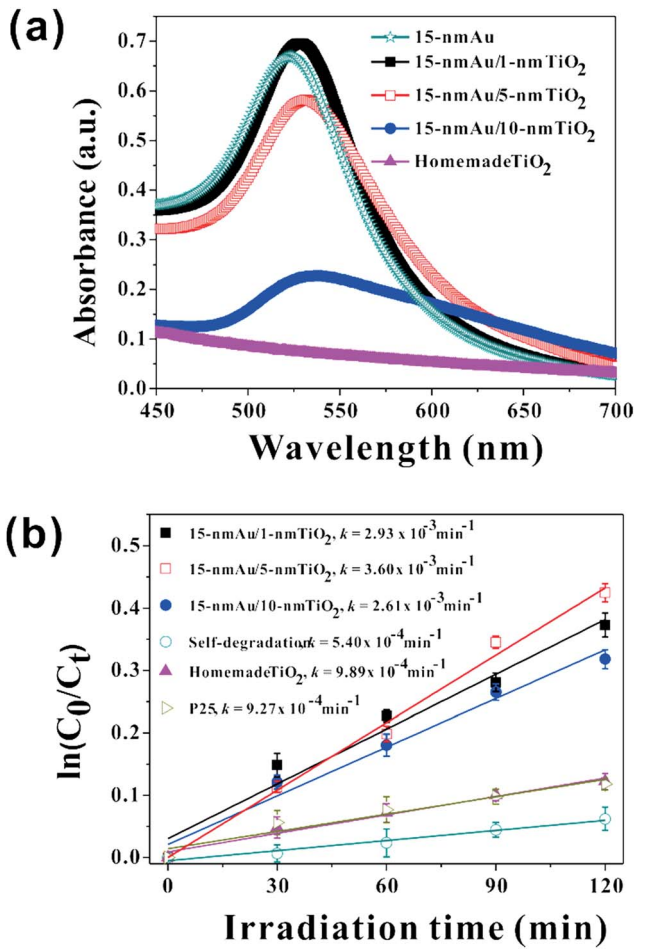

Fig. 4 (a) Optical absorption spectra of P*t*BA-*b*-PEO-capped Au nanoparticles, homemade PEO-capped TiO_2 nanoparticles, and PEO-capped Au/TiO_2 core/shell nanoparticles with a fixed diameter of the Au core and varied thickness of the TiO_2 shell. (b) Photocatalytic degradation rates of RhB under visible light irradiation using the samples noted in (a) after calcination at 500 °C in air (*i.e.*, removal of PEO) as well as the P25 sample.

enhancement in the overall refractive index of the medium encapsulating the Au core, which in turn promoted the dielectric effect and led to a more pronounced red-shift in the plasmonic peak of Au (*i.e.*, from 528 nm for the 1 nm thick shell, to 531.5 nm for the 5 nm thick shell, and to 538.5 nm for the 10 nm thick shell (Fig. 4a)).[23]

The photocatalytic activities of Au/TiO_2 nanoparticles were assessed through the photodegradation of RhB aqueous solution under visible light irradiation (Fig. 4b). Each dataset was measured 5 times. The average value of each experimental result and the corresponding error bars are shown in Fig. 4b. Intriguingly, in this work, the PEO chains on the surface of the nanoparticles were found to physically adsorb RhB and trap RhB around Au/TiO_2 nanoparticles without being actually degraded (Fig. S2†). Such a dense layer of RhB surrounding Au/TiO_2 nanoparticles hindered the absorbance of incident light by the nanoparticles. It has been reported that the capping ligands on the surface of photocatalysts need to be removed prior to their use in photocatalytic applications.[24] Therefore, the calcination at 500 °C in air was performed to remove PEO chains, and in the meantime the amorphous TiO_2 shell was converted into the anatase phase, which is more favorable for photocatalysis. It is worth noting that the Au core was separated from RhB by the TiO_2 shell, thus eliminating the chemical catalysis effect of Au nanoparticles.[25] It is well known that thermal plasmonic heating can be generated by Au nanoparticles under visible light irradiation. However, the photocatalytic reaction caused by thermal plasmonic heating does not generally occur.[13,25,26] This is due to the quick heat dissipation by the solution (and the TiO_2 shell encapsulating the Au core as in this work) before the degradation reaction starts.

The degradation of RhB can be described by a pseudo-first-order reaction with a simplified Langmuir–Hinshelwood model, given as $\ln(C/C_0) = |k|t$, where C and C_0 are the reaction and initial concentrations of RhB, respectively, and $|k|$ is the apparent first-order reaction constant. As shown in Fig. 4b, the degradation constants, $|k|$, of P25, homemade 10 nm TiO_2 nanoparticles (Fig. S3†), Au/TiO_2 nanoparticles with a 15 nm Au core and the varied TiO_2 shell thickness of 1 nm, 5 nm and 10 nm are 9.27×10^{-4} min^{-1}, 9.89×10^{-4} min^{-1}, 2.93×10^{-3} min^{-1}, 3.60×10^{-3} min^{-1}, and 2.61×10^{-3} min^{-1}, respectively. Clearly, Au/TiO_2 core/shell nanoparticles exhibited higher photocatalytic activity than homemade TiO_2 nanoparticles and P25. The improved photocatalytic performances can be rationalized as follows. First, the enhanced light harvesting was enabled by surface plasmon absorption of the Au core. Second, the Schottky junction, formed upon the contact of the metal and semiconductor, established an internal electric field close to the metal/semiconductor interface and led to the transfer of the photogenerated electrons and holes from Au to TiO_2.[27] Finally, the tunable thickness of the TiO_2 shell was comparable to the carrier diffusion length, which was a few nanometers. Thus, the photogenerated charge carriers can effectively transfer to the surface of TiO_2 in Au/TiO_2 core/shell photocatalysts,[28] which minimized or suppressed the electron–hole recombination, thereby further improving the photocatalytic activity. Surprisingly, Au/TiO_2 nanoparticles with 5 nm shell thickness exhibited the optimal photocatalytic performance, and possessed the highest $|k|$, which is approximately 3.6 ($3.60 \times 10^{-3}/(9.89 \times 10^{-4}) = 3.6$), 3.88 ($3.60 \times 10^{-3}/(9.27 \times 10^{-4}) = 3.9$) times larger than that of the homemade TiO_2 and P25, respectively. Au/TiO_2 nanoparticles with the 10 nm thick shell had less specific surface area, that is, less adsorption capacity of RhB in comparison to the other two core/shell samples, as the identical amount of the three different Au/TiO_2 nanoparticle samples was used in the study. Moreover, the plasmonic near-fields are localized close to the Au/TiO_2 interface, and thus most of the electron–hole pairs are generated in close proximity to the interface.[13] Therefore, for Au/TiO_2 nanoparticles with a thicker shell, photogenerated electrons had to migrate longer distance before reaching the TiO_2 surface for photocatalytic degradation of RhB, which in turn increased the charge recombination. It is thus understandable that 15 nm Au/10 nm TiO_2 nanoparticles possessed relatively low photocatalytic activity. Notably, compared to the sample with 5 nm TiO_2 shell thickness as described above, Au/TiO_2 nanoparticles with 1 nm thickness also demonstrated comparatively low photocatalytic performance. The conduction band (CB) of TiO_2 is located lower than the oxidation potential of RhB. Therefore, the excited RhB can quickly inject electrons into the CB of TiO_2, which accelerated the degradation of RhB.[29] Despite that the sample with 1 nm TiO_2 shell thickness had a larger specific surface area, it suffered from comparatively low photocatalytic activity due to the presence of a small amount of TiO_2 as the equal weight of three different Au/TiO_2 core/shell samples was added to the photoreactor. Taken together, 15 nm Au/5 nm TiO_2 nanoparticles stood out as the best photocatalyst among them.

In this context, we fixed the TiO_2 shell thickness at 5 nm and systematically altered the Au core diameter (*i.e.*, 5 nm, 10 nm and 15 nm in Fig. 2c, d and 1c, respectively) to scrutinize the size effect of the Au core on photocatalysis. All PEO-capped Au/TiO_2 nanoparticles exhibited the LSPR peaks in the visible light region (Fig. 5a). We note that the corresponding P*t*BA-*b*-PEO-capped Au nanoparticles (lower right panel in Scheme 1) prior to the formation of PEO-capped Au/TiO_2 nanoparticles (lower left panel in Scheme 1) were also prepared and used as controls. Similarly, in comparison with 5 nm, 10 nm and 15 nm P*t*BA-*b*-PEO-capped Au nanoparticles with the LSPR position centered in the range of 520–525 nm (solid square curve, solid star curve, and open star curve, respectively, in Fig. 5a), the red-shift was seen on the LSPR peaks of Au/TiO_2 nanoparticles due to the change of dielectric environment (*i.e.*, the deposition of higher-refractive-index TiO_2 shell). With the increase in the Au core diameter (from 5 nm to 15 nm) at the fixed TiO_2 shell thickness (5 nm), the LSPR position of Au/TiO_2 nanoparticles essentially remained nearly constant (approximately 532 nm; Fig. 5a) due to the presence of the same thickness of TiO_2 shell (*i.e.*, same dielectric effect).

Likewise, photocatalytic performances of Au/TiO_2 nanoparticles with varied diameter of Au core and fixed thickness of TiO_2 shell in the degradation of RhB were examined. Fig. 5b presents the linear relationship of $\ln(C/C_0)$ as a function of the photocatalytic time. Obviously, Au/TiO_2 nanoparticles outperformed homemade TiO_2 nanoparticles (diameter = 10 nm)

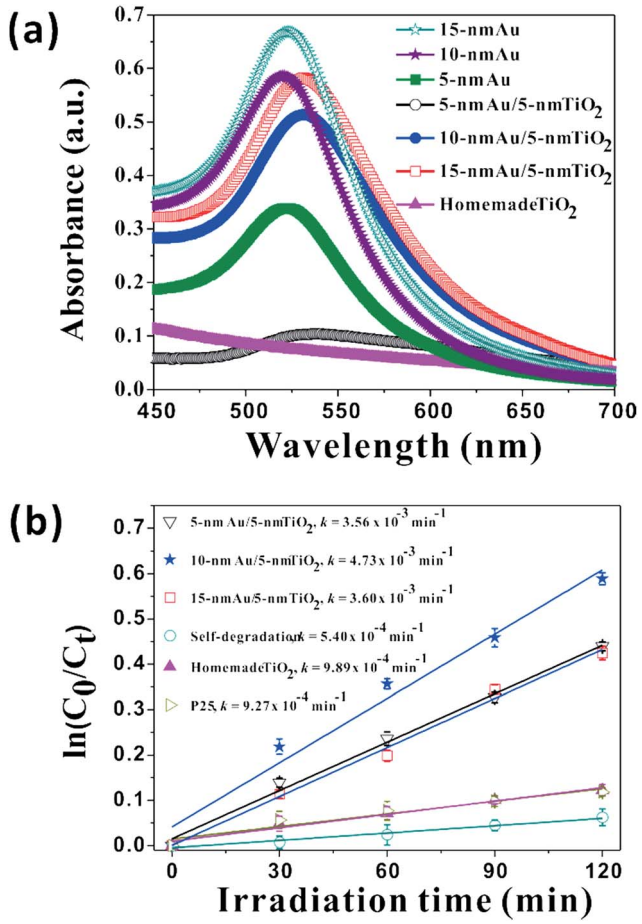

Fig. 5 (a) Optical absorption spectra of P*t*BA-*b*-PEO-capped Au nanoparticles, homemade PEO-capped TiO_2 nanoparticles, and PEO-capped Au/TiO_2 core/shell nanoparticles with the varied diameter of Au core and the constant thickness of TiO_2 shell. (b) Photocatalytic degradation rates of RhB under visible light irradiation using the samples noted in (a) after calcination at 500 °C in air (*i.e.*, removal of PEO) as well as the P25 sample.

and P25 under visible light irradiation. The degradation rates of RhB for Au/TiO_2 nanoparticles with Au core diameters of 5 nm, 10 nm and 15 nm were 3.56×10^{-3} min^{-1}, 4.73×10^{-3} min^{-1} and 3.60×10^{-3} min^{-1}, respectively. Au/TiO_2 nanoparticles with a 10 nm Au core emerged as the most efficient photocatalyst and had a $|k|$ that was 4.8 ($4.73 \times 10^{-3}/(9.89 \times 10^{-4}) = 4.8$) and 5.1 ($4.73 \times 10^{-3}/(9.27 \times 10^{-4}) = 5.1$) times that of homemade TiO_2 and P25. The relatively lower efficiency in the degradation of RhB for Au/TiO_2 core/shell photocatalysts with the 5 nm Au core can be ascribed to the less photoinduced electron–hole pairs caused by the relatively weak plasmonic effect due to the smaller diameter of the Au core (5 nm as opposed to 10 nm or 15 nm).[30] On the other hand, for Au/TiO_2 nanoparticles with a 15 nm Au core, their relatively lower performance was due likely to the less specific surface area of Au/TiO_2 nanoparticles as the same amount of samples was used in the degradation of RhB, as discussed above.

We now turn our attention to further understand the enhanced plasmonic-driven photocatalysis *via* employing

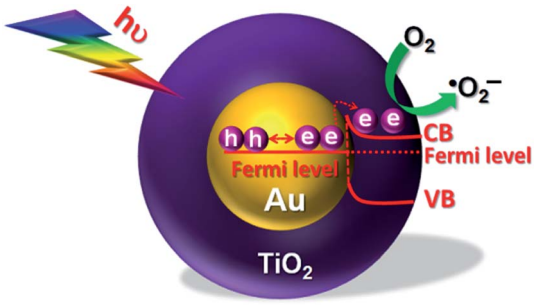

Scheme 2 Schematic illustration of the mechanism of photocatalytic degradation of RhB by employing Au/TiO_2 core/shell nanoparticles as photocatalysts under visible light irradiation.

uniform and precisely size-controllable plasmonic/semiconducting Au/TiO_2 core/shell nanoparticles as photocatalysts. As the TiO_2 shell was in close contact with the Au core, the electrons diffused from n-type TiO_2 to Au, forming a positively charged region with no free carriers in the TiO_2 shell, and thus creating a space-charge region. In the meantime, an equal amount of electrons were confined on the surface of the Au core. Thus, an internal electrical field was built up from TiO_2 toward Au. Upon the irradiation of Au/TiO_2 photocatalysts by the incident light, the internal electric field promoted photogenerated electrons in or near the space-charge region to move to TiO_2, and the holes to Au, thereby suppressing the electron–hole recombination dynamics. Moreover, it is worth noting that in this work, direct electron transfer was facilitated due to the intimate contact between the Au core and the TiO_2 shell in Au/TiO_2 nanoparticles enabled by the star-like block copolymer nanoreactor strategy, thereby rendering efficient photocatalytic degradation of RhB. The band diagram for a Schottky barrier formed upon the contact of Au and TiO_2 is depicted in Scheme 2. Under the visible light irradiation, surface plasmons were excited in the Au core and decayed into hot electron–hole pairs.[31] The hot electrons instantaneously occupied the empty conduction band (CB) of Au above its Fermi level.[31] Because of the intimate contact of Au and TiO_2, the majority of hot electrons transferred to the CB of TiO_2 by overcoming the Schottky barrier at the Au/TiO_2 interface, and subsequently migrated to the surface of TiO_2.[31] The oxygen adsorbed on the surface of Au/TiO_2 core/shell photocatalysts reacted with these electrons to form the superoxide radical anion, which underwent further reactions to form the hydroxyl radicals.[29] Due to the photosensitization effect, RhB adsorbed on Au/TiO_2 nanoparticles yielded RhB^+.[29] The hydroxyl radicals with strong oxidation ability eventually mineralized RhB^+.[32]

Conclusions

In summary, by judiciously capitalizing on the amphiphilic star-like P4VP-*b*-P*t*BA-*b*-PEO triblock copolymer as a nanoreactor that was rationally designed and synthesized *via* combining sequential ATRP with a click reaction, uniform core/shell nanoparticles composed of a plasmonic Au core and semiconductor TiO_2 shell with precisely adjustable dimensions were

nonepitaxially crafted. These plasmonic/semiconducting core/shell nanoparticles were exploited as photocatalysts. Their photocatalytic activities were several fold higher than those of homemade TiO_2 nanoparticles and P25, which was due primarily to the enhanced light harvesting enabled by the LSPR of the Au core and the built-in internal electric field. Quite interestingly, the 10 nm Au/5 nm TiO_2 core/shell nanoparticles were found to exert the highest degradation rate of RhB under visible light irradiation.

The nonepitaxial growth strategy is facile and robust, and can be readily extended to create a myriad of other functional core/shell nanoparticles as the core and shell materials are independently grown, thereby dispensing with the need for lattice match between two disparate materials. It represents a particularly promising technique that offers new levels of tailorability in the dimensions, compositions and architectures of nanomaterials. As a diversity of materials are amenable to such nonepitaxial growth reaction, the markedly different nanomaterials crafted would render the exploration of the fundamental size-dependent optical, electronic, optoelectronic, magnetic, catalytic and sensory properties for a wide range of applications in advanced catalysis, chemical sensors, energy conversion and storage, electronics, nanotechnology, and biotechnology.

Acknowledgements

We gratefully acknowledge funding support from the Air Force Office of Scientific Research (FA9550-13-1-0101) (Z. L.), National Science Foundation (ECCS-1305087) (Z. L.), National Basic Research Program of China (2012CB932900) (C. L.), National Natural Science Foundation of China (21321062) (C. L. and L. S.), and the China Scholarship Council (M. W.). We thank Younan Xia for discussion.

References

1 X. Pang, L. Zhao, W. Han, X. Xin and Z. Lin, A general and robust strategy for the synthesis of nearly monodisperse colloidal nanocrystals, *Nat. Nanotechnol.*, 2013, **8**, 426–431.
2 Z. Wang, Transmission electron microscopy of shape-controlled nanocrystals and their assemblies, *J. Phys. Chem. B*, 2000, **104**, 1153–1175.
3 C. Palmstrom, Epitaxy of dissimilar materials, *Annu. Rev. Mater. Sci.*, 1995, **25**, 389–415.
4 M. Pang, J. Hu and H. C. Zeng, Synthesis, morphological control, and antibacterial properties of hollow/solid Ag2S/Ag heterodimers, *J. Am. Chem. Soc.*, 2010, **132**, 10771–10785.
5 M. Wang, J. Iocozzia, L. Sun, C. Lin and Z. Lin, Semiconductor TiO_2 nanotube arrays for photocatalysis, *Energy Environ. Sci.*, 2014, **7**, 2182–2202.
6 H. A. Atwater and A. Polman, Plasmonics for improved photovoltaic devices, *Nat. Mater.*, 2010, **9**, 205–213.
7 P. Alivisatos, The use of nanocrystals in biological detection, *Nat. Biotechnol.*, 2003, **22**, 47–52.
8 X. Qian, X.-H. Peng, D. O. Ansari, Q. Yin-Goen, G. Z. Chen, D. M. Shin, L. Yang, A. N. Young, M. D. Wang and S. Nie, *In vivo* tumor targeting and spectroscopic detection with surface-enhanced Raman nanoparticle tags, *Nat. Biotechnol.*, 2007, **26**, 83–90.
9 Y. Li, Y. Wu and B. S. Ong, Facile synthesis of silver nanoparticles useful for fabrication of high-conductivity elements for printed electronics, *J. Am. Chem. Soc.*, 2005, **127**, 3266–3267.
10 M. Noginov, G. Zhu, A. Belgrave, R. Bakker, V. Shalaev, E. Narimanov, S. Stout, E. Herz, T. Suteewong and U. Wiesner, Demonstration of a spaser-based nanolaser, *Nature*, 2009, **460**, 1110–1112.
11 M. Ye, J. Gong, Y. Lai, C. Lin and Z. Lin, High-efficiency photoelectrocatalytic hydrogen generation enabled by palladium quantum dots-sensitized TiO_2 nanotube arrays, *J. Am. Chem. Soc.*, 2012, **134**, 15720–15723.
12 K. Wu, W. E. Rodríguez-Córdoba, Y. Yang and T. Lian, Plasmon-induced hot electron transfer from the Au tip to CdS rod in CdS-Au nanoheterostructures, *Nano Lett.*, 2013, **13**, 5255–5263.
13 Z. W. Seh, S. Liu, M. Low, S. Y. Zhang, Z. Liu, A. Mlayah and M. Y. Han, Janus Au-TiO_2 photocatalysts with strong localization of plasmonic near-fields for efficient visible-light hydrogen generation, *Adv. Mater.*, 2012, **24**, 2310–2314.
14 Y.-C. Pu, G. Wang, K.-D. Chang, Y. Ling, Y.-K. Lin, B. C. Fitzmorris, C.-M. Liu, X. Lu, Y. Tong and J. Z. Zhang, Au Nanostructure-decorated TiO_2 nanowires exhibiting photoactivity across entire UV-visible region for photoelectrochemical water splitting, *Nano Lett.*, 2013, **13**, 3817–3823.
15 J. Zhang, Y. Tang, K. Lee and M. Ouyang, Nonepitaxial growth of hybrid core–shell nanostructures with large lattice mismatches, *Science*, 2010, **327**, 1634–1638.
16 Q. Zhang, W. Li, C. Moran, J. Zeng, J. Chen, L.-P. Wen and Y. Xia, Seed-mediated synthesis of Ag nanocubes with controllable edge lengths in the range of 30–200 nm and comparison of their optical properties, *J. Am. Chem. Soc.*, 2010, **132**, 11372–11378.
17 Z. Li, P. Li and J. Huang, Synthesis of amphiphilic copolymer brushes: poly(ethylene oxide)-graft-polystyrene, *J. Polym. Sci., Part A: Polym. Chem.*, 2006, **44**, 4361–4371.
18 X. C. Pang, L. Zhao, M. Akinc, J. K. Kim and Z. Q. Lin, Novel amphiphilic multi-arm, star-like block copolymers as unimolecular micelles, *Macromolecules*, 2011, **44**, 3746–3752.
19 X. C. Pang, L. Zhao, C. W. Feng, R. F. Wu, H. H. Ma and Z. Q. Lin, Functional copolymer brushes composed of a hydrophobic backbone and densely grafted conjugated side chains *via* a combination of living polymerization with click chemistry, *Polym. Chem.*, 2013, **4**, 2025–2032.
20 X. C. Pang, L. Zhao, C. W. Feng and Z. Q. Lin, Novel amphiphilic multiarm, starlike coil-rod diblock copolymers *via* a combination of click chemistry with living polymerization, *Macromolecules*, 2011, **44**, 7176–7183.
21 S. E. Stiriba, H. Frey and R. Haag, Dendritic polymers in biomedical applications: from potential to clinical use in diagnostics and therapy, *Angew. Chem., Int. Ed.*, 2002, **41**, 1329–1334.

22 X. Zhang, Y. L. Chen, R.-S. Liu and D. P. Tsai, Plasmonic photocatalysis, *Rep. Prog. Phys.*, 2013, **76**, 046401.
23 W.-T. Chen, T.-T. Yang and Y.-J. Hsu, Au-CdS core–shell nanocrystals with controllable shell thickness and photoinduced charge separation property, *Chem. Mater.*, 2008, **20**, 7204–7206.
24 H. Tong, S. Ouyang, Y. Bi, N. Umezawa, M. Oshikiri and J. Ye, Nano-photocatalytic materials: possibilities and challenges, *Adv. Mater.*, 2012, **24**, 229–251.
25 S. K. Cushing, J. Li, F. Meng, T. R. Senty, S. Suri, M. Zhi, M. Li, A. D. Bristow and N. Wu, Photocatalytic activity enhanced by plasmonic resonant energy transfer from metal to semiconductor, *J. Am. Chem. Soc.*, 2012, **134**, 15033–15041.
26 W. H. Hung, M. Aykol, D. Valley, W. B. Hou and S. B. Cronin, Plasmon resonant enhancement of carbon monoxide catalysis, *Nano Lett.*, 2010, **10**, 1314–1318.
27 Z. Wang, J. Liu and W. Chen, Plasmonic Ag/AgBr nanohybrid: synergistic effect of SPR with photographic sensitivity for enhanced photocatalytic activity and stability, *Dalton Trans.*, 2012, **41**, 4866–4870.
28 S. Linic, P. Christopher and D. B. Ingram, Plasmonic-metal nanostructures for efficient conversion of solar to chemical energy, *Nat. Mater.*, 2011, **10**, 911–921.
29 M. Wang, L. Sun, Z. Lin, J. Cai, K. Xie and C. Lin, p–n Heterojunction photoelectrodes composed of Cu_2O-loaded TiO_2 nanotube arrays with enhanced photoelectrochemical and photoelectrocatalytic activities, *Energy Environ. Sci.*, 2013, **6**, 1211–1220.
30 S. Berciaud, L. Cognet, P. Tamarat and B. Lounis, Observation of intrinsic size effects in the optical response of individual gold nanoparticles, *Nano Lett.*, 2005, **5**, 515–518.
31 X. Zhang, Y. Liu, S.-T. Lee, S. Yang and Z. Kang, Coupling surface plasmon resonance of gold nanoparticles with slow-photon-effect of TiO_2 photonic crystals for synergistically enhanced photoelectrochemical water splitting, *Energy Environ. Sci.*, 2014, **7**, 1409–1419.
32 M. Wang, L. Sun, J. Cai, P. Huang, Y. Su and C. Lin, A facile hydrothermal deposition of $ZnFe_2O_4$ nanoparticles on TiO_2 nanotube arrays for enhanced visible light photocatalytic activity, *J. Mater. Chem. A*, 2013, **1**, 12082–12087.